



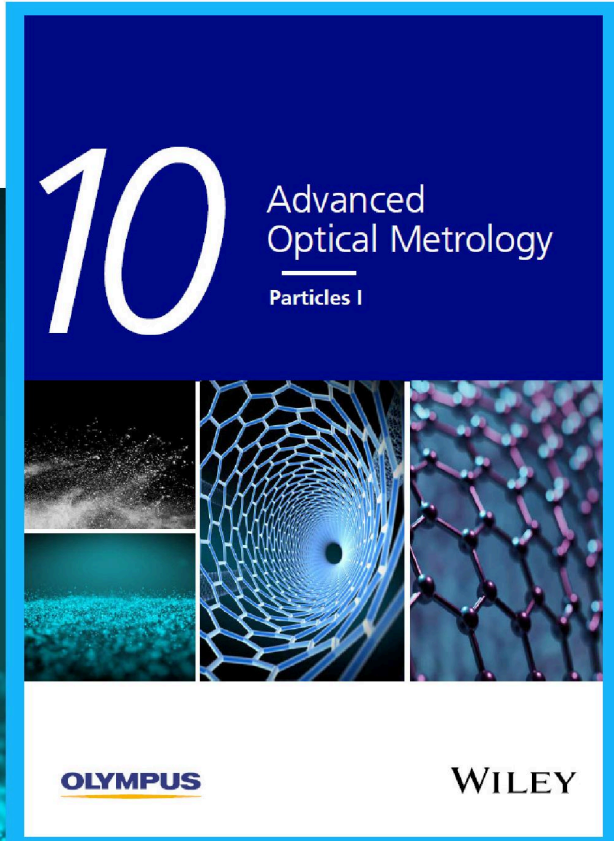
Particles I

Access the latest eBook →

Particles: Unique Properties,
Uncountable Applications

**Read the latest eBook and
better your knowledge with
highlights from the recent
studies on the design and
characterization of micro-
and nanoparticles for
different application areas.**

Access Now



This eBook is sponsored by

OLYMPUS[®]

WILEY

Beyond Skin Pressure Sensing: 3D Printed Laminated Graphene Pressure Sensing Material Combines Extremely Low Detection Limits with Wide Detection Range

Kunli Cao, Miao Wu, Jiabao Bai, Zhen Wen, Jianwei Zhang, Tianyi Wang, Meiwen Peng, Tao Liu, Zheng Jia, Zhiqiang Liang,* and Lin Jiang*

Artificial intelligence robots predicted in sci-fi movies have attracted increasing attention in recent years, and much effort has been devoted to improving the sensing and manipulation performance of robots. The development of robotic skins capable of handling complex external pressure environments is highly desired for intelligent robots. However, this remains a major challenge due to the lack of pressure sensing materials that can combine extremely low detection limits and wide detection ranges. Inspired by the synergistic strategy of dual mechanoreceptors in human skin, here, the design and 3D printing of laminated graphene pressure sensing materials consisting of both ultrathin- and thick-walled cellular microstructures are demonstrated. Based on such laminated graphene, the piezoresistive pressure sensor achieves a low detection limit of 1 Pa, a wide detection range (1 Pa–400 kPa), and high sensitivities of 3.1 and 0.22 kPa⁻¹ in the pressure regions of 1 Pa–13 kPa and 13–400 kPa, respectively, and the laminated graphene-based skin enables quantitative pressure/weight detection. This laminated graphene can be easily integrated into flexible pressure sensing arrays that enable mapping the spatial distribution of pressure, showing great potential for applications such as electronic skin, physiological signal monitoring, and human–machine interfaces.

1. Introduction

The combination of artificial intelligence (AI) and robotics has become one of the fastest-growing branches of science and technology and is considered to have a profound impact on human society. For example, in recent decades, the artificially intelligent

robots predicted in sci-fi movies have attracted increasing attention, and considerable effort has been devoted to studying the enhancement of perception and object manipulation capabilities of intelligent robots.^[1–9] To mimic, or even beyond, the functions of a human hand, a robotic hand needs to be able to handle a complex surrounding pressure environment in practical applications. It has been demonstrated that the excellent pressure perception ability of the human hands is derived from a particularly interesting feature of the synergistic strategy of touch receptors and baroreceptors in human skin.^[10,11] The touch receptors grown in the superficial layer of the human skin are sensitive to subtle pressure (down to ≈1 Pa), while the baroreceptors (torus corpuscle) in the deeper layer of the skin can endure and sense a large external pressure (100–300 kPa).^[12–15] The synergy of touch receptors and baroreceptors allows human skin to sensitively convert both subtle and high-pressure stimuli into biological signals. As the interface between


the robots and the surrounding environment, the pressure sensing components of robot skin is also expected to be sensitive to both subtle (e.g., gentle breeze and touch) and high-pressure stimuli,^[16,17] enabling intelligent robots to achieve precise manipulations. Nevertheless, one of the main reasons behind the absence of domestic robots from everyday life is unmet pressure sensing requirements, that is, the lack of a robotic skin equivalent to or even beyond human skin.^[18,19] Therefore, it is highly desirable to develop pressure sensing materials with both extremely low detection limits and wide detection ranges to create robotic skins comparable to or even exceeding human skin.

Among the various types of pressure sensors, piezoresistive sensors, which can directly convert the applied pressure into an electrical signal, have attracted tremendous attention because of their simple structure, feasible fabrication, high sensitivity, ability to detect both static and dynamic deformation, and ease of system integration and signal acquisition.^[20–24] It has been demonstrated that the change in contact areas/points of conductive sensing materials under applied pressure significantly determines the electrical properties of the pressure sensing materials. Therefore, in recent years, much effort has been

K. Cao, M. Wu, Z. Wen, J. Zhang, T. Wang, M. Peng, Z. Liang, L. Jiang
Institute of Functional Nano and Soft Materials Laboratory (FUNSOM)
and Jiangsu Key Laboratory for Carbon-Based Functional Materials and
Devices

Soochow University
Suzhou, Jiangsu 215123, P. R. China
E-mail: zqliang@suda.edu.cn; ljiang@suda.edu.cn

J. Bai, T. Liu, Z. Jia
Department of Engineering Mechanics
Zhejiang University
Hangzhou, Zhejiang 310027, P. R. China

 The ORCID identification number(s) for the author(s) of this article can be found under <https://doi.org/10.1002/adfm.202202360>.

DOI: 10.1002/adfm.202202360

devoted to constructing materials into delicate microstructures with low modulus, enabling them to respond sensitively to subtle pressure stimuli.^[25–30] However, the low modulus and fragile nature of these microstructures make them unable to withstand and detect large pressures. In contrast, high-modulus materials are capable of producing sufficient deformation at high pressures to enable the detection of high pressures, but their mechanical properties prevent them from responding to ultralow pressure.^[31,32] To date, most of the reported skin-mimicking pressure sensing materials have always been limited to mimicking a single microstructure, resulting in none of them reaching a pressure-sensing range comparable to that of human skin.^[1,33] The development of pressure-sensing materials with both low detection limits and wide detection ranges remains a major challenge (Table S1, Supporting Information).

Inspired by the synergistic effect of dual mechanoreceptors in human skin, we suggest that the integration of well-designed microstructures with different pressure-sensitive properties has great potential in addressing the contradiction between the ultralow detection limit and high-pressure detection capability that cannot be combined via a single microstructure. However, the problem of poor interfacial bonding often arises when materials with different microstructures are laminated together using conventional material preparation methods.

How to reliably integrate different microstructures into pressure sensing materials with controllable shape and size and to better mimic the synergy of dual mechanoreceptors to allow the pressure-sensing components for intelligent robots to meet or even beyond the pressure-sensing ability of human skin (Figure 1a) remains a significant challenge.

Herein, inspired by the dual mechanoreceptors in human skin (Figure 1b), we demonstrated the design and 3D printing of laminated graphene pressure sensing materials consisting of both ultrathin-walled and thick-walled cellular microstructured layers (Figure 1c). The excellent flexibility and controllability of ink-based 3D printing allow us to print different microstructures into seamlessly laminated graphene material. Note that to enable the 3D printing of laminated graphene materials, a family of carbomer hydrogel-based reduced graphene oxide (H-RGO) inks with excellent rheological properties and tunable solid contents were developed. In particular, based on this hydrogel-based ink preparation strategy, we have achieved for the first time an aqueous-based graphene ink with ultralow solid content (down to 3 mg mL⁻¹) and meeting the requirements of direct-ink-writing (DIW) 3D printing. In the laminated graphene materials, the ultrathin-walled cellular layer (Figure 1e, top) and thick-walled cellular layer (Figure 1e, bottom) are printed by using H-RGO inks with ultralow

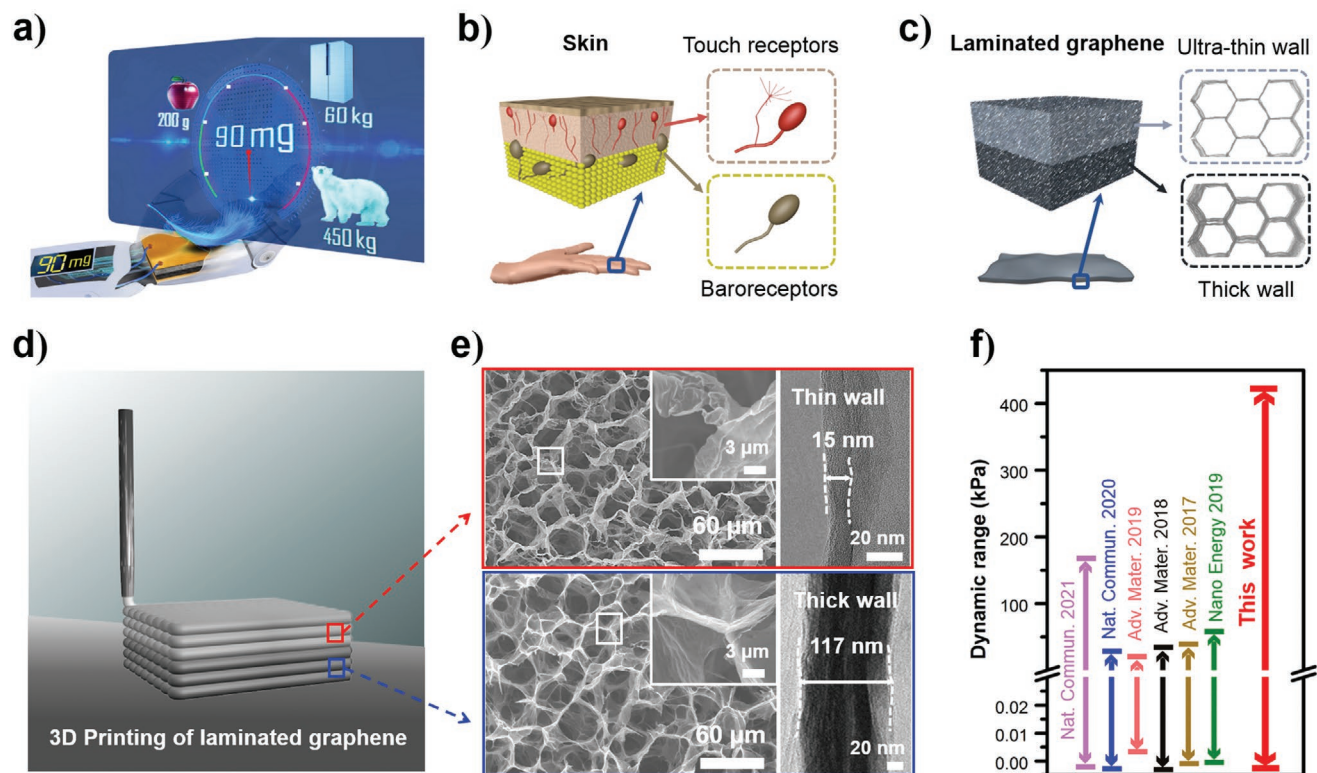


Figure 1. 3D printed laminated graphene pressure sensing materials with different cellular microstructures. a) A robotic hand with an ideal pressure sensing unit capable of quantitatively sensing external pressure stimuli over a wide pressure range. b) Schematic diagram of the biological microstructure of human skin, showing touch receptors and baroreceptors. c) Schematic demonstration of the structure of laminated graphene. Ultrathin-walled cellular graphene layer (top) and thick-walled cellular graphene layer (bottom). d) 3D printing of laminated graphene materials using H-RGO inks. e) Cross-sectional scanning electron microscopy (SEM) images and transmission electron microscopy (TEM) images of 3D printed laminated graphene, which show that the ultrathin-walled cellular layer has an ultrathin wall thickness of ≈ 15 nm (top), while the thick-walled cellular layer has a wall thickness of ≈ 117 nm (bottom). f) Extremely low detection limits and wide detection range of pressure sensors based on laminated graphene and their comparison with the representative carbon-based pressure sensors reported in the literature.^[34–39] (nonexhaustive survey).

(3 mg mL⁻¹) and relatively high (25 mg mL⁻¹) graphene contents, respectively. The soft ultrathin-walled cellular (Figure 1c, top) is designed to function as the touch receptor in the human skin (Figure 1b, top) and to detect gentle pressure stimuli, while the thick-walled cellular (Figure 1c, bottom) with high elastic modulus is used to serve as the baroreceptors in the skin (Figure 1b, bottom) to sense high-pressure stimuli. As a result, pressure sensors based on such laminated sensing materials simultaneously achieve extremely low detection limits down to 1 Pa, a wide detection range (1 Pa–400 kPa), and high sensitivities of 3.1 and 0.22 kPa⁻¹ in the pressure regions of 1 Pa–13 kPa and 13–400 kPa, respectively. To the best of our knowledge, this is the first demonstration of a carbon-based pressure sensor that goes beyond the pressure sensing range of human skin (Figure 1f). The laminated graphene pressure sensor exhibits the ability to quantify pressure/weight over a wide range. In addition, the cellular microstructure and the ultrathin polydimethylsiloxane (PDMS) coating on the surface of the cellular well impart excellent elasticity and stability to the laminated graphene, which enables the sensor to hold excellent stability up to 10000 cycles of testing. Moreover, we demonstrated the feasibility of this laminated graphene pressure-sensing material for integrating large-area electronic skins, demonstrating the potential to enable AI robots to quantitatively sense the weight of objects for precise manipulation. This skin-inspired design concept of laminated pressure sensing materials combined with 3D printing technology provides a promising strategy for meeting the demands of AI robots for the sensitive perception of complex pressure environments.

2. Results and Discussion

To fabricate skin-inspired laminated graphene pressure sensing materials, an extrusion-based 3D printing technology, also named the DIW method, was explored to integrate different microstructures into laminated structures. The excellent flexibility and controllability of the 3D printing approach enable the building of laminated graphene with a designed shape and size. In addition, the continuous layer-by-layer printing process makes the interface between the different microstructure layers well bonded, which is difficult to achieve by conventional fabrication methods.

The development of printable inks with suitable viscoelasticity is a prerequisite for ink-based 3D printing technology. Note that to achieve skin-like detection of weak pressure, a soft (low modulus) graphene material with ultralow density needs to be printed so that sufficient deformation can occur at very low applied pressures. Unfortunately, traditional graphene-based inks for extrusion-based 3D printing approach always require high solid contents (ranging from 20–100 mg mL⁻¹),^[40–44] making it difficult to obtain ultralow density and soft mechanical properties. This is because conventional aqueous-based graphene inks require a high solid content to obtain an adequate storage modulus (G') and yield stress (τ_y) to enable the self-supporting ability of the ink filaments during the 3D printing process. In view of this, in this work, we developed a family of carbomer hydrogel-based graphene ink to overcome the dependence of conventional graphene inks on high solid content.

Carbomer is a cross-linked acrylic acid polymer whose molecules appear in curled clusters in water. The carboxyl groups in the carbomer molecule will partially decompose into hydrogen ions and carboxylate anions in water, making the aqueous solution of carbomer slightly acidic. The addition of NaOH to the aqueous solution of carbomer to adjust the pH to neutral can cause further ionization of the carboxyl groups in the curled carbomer molecules. Eventually, the carbomer molecules swell under the repulsive force of the negatively charged groups (–COO⁻) and form a microgel with a 3D network structure.^[45] The supporting ability of the network of carbomer molecules in hydrogels enables the preparation of 3D printable H-RGO inks with ultralow graphene content (3 mg mL⁻¹) (Figure 2a).

Prior to the preparation of H-RGO inks, large lateral-sized GO nanosheets with lateral sizes in the range of $\approx 5 \mu\text{m}$ to tens of microns and a thickness of $\approx 1.5 \text{ nm}$ (Figure S1, Supporting Information) were prepared first by a modified Hummers method.^[46] The GO suspensions were then reduced using ascorbic acid (AA) as a weak reductant (see Experimental Section for details). It has been demonstrated that by controlling the reduction of GO in the ink, the cross-linked GO nanosheets can be assembled into cellular microstructures via a freeze casting treatment under the extrusion of ice crystals.^[47–49] Note that the porous microstructure undergoes a significant change in contact area under external pressure, which in turn leads to changes in electrical properties, making it suitable for preparing high-performance pressure sensors.^[50,51] After pre-reduction, the partially reduced GO (pr-GO) suspension was then homogeneously mixed with the carbomer. Then, the H-RGO inks were obtained by gelation of the mixture. To obtain ultrathin-walled and thick-walled cellular structured graphene, we prepared two kinds of H-RGO inks with ultralow (3 mg mL⁻¹) and relatively higher (25 mg mL⁻¹) graphene contents.

The rheological properties of H-RGO inks with graphene loadings of 3 and 25 mg mL⁻¹ were recorded and are presented in Figure 2b–d. As shown in Figure 2b, the apparent viscosity of all the inks decreases approximately linearly with increasing shear rate from 10^1 to 10^3 s^{-1} on a logarithmic scale, evidencing their pronounced shear-thinning behavior. The shear-thinning behavior indicates that these inks could be smoothly extruded out through the fine nozzles under a suitable printing pressure.^[52] In addition to shear-thinning behavior, the high G' and τ_y are also crucial for the self-supporting nature of the ink filaments as well as the printed 3D structures. Figure 2c presents the G' and loss modulus (G'') of the H-RGO inks as a function of the shear stress on a logarithmic scale. Note that G' and G'' reflect the elastic and viscous properties of the ink, respectively.^[53,54] Figure 2c shows that both of the H-RGO inks with graphene contents of 3 and 25 mg mL⁻¹ have high G' plateaus of $\approx 2 \times 10^3$ and $\approx 1 \times 10^4 \text{ Pa}$, respectively. Moreover, the G' plateaus are significantly higher than their G'' plateaus, which is also important to enable the shape retention and self-supporting ability of the newly printed 3D structures during the printing process.^[55–57]

To evaluate the stability of the H-RGO inks, the evaluation of both G' and G'' as a function of time for the inks with graphene contents of 3 and 25 mg mL⁻¹ were recorded and are presented in Figure 2d. Both inks showed no significant change in moduli with test time, showing excellent stability. By optimizing the printing parameters, including printing pressure and speed, we

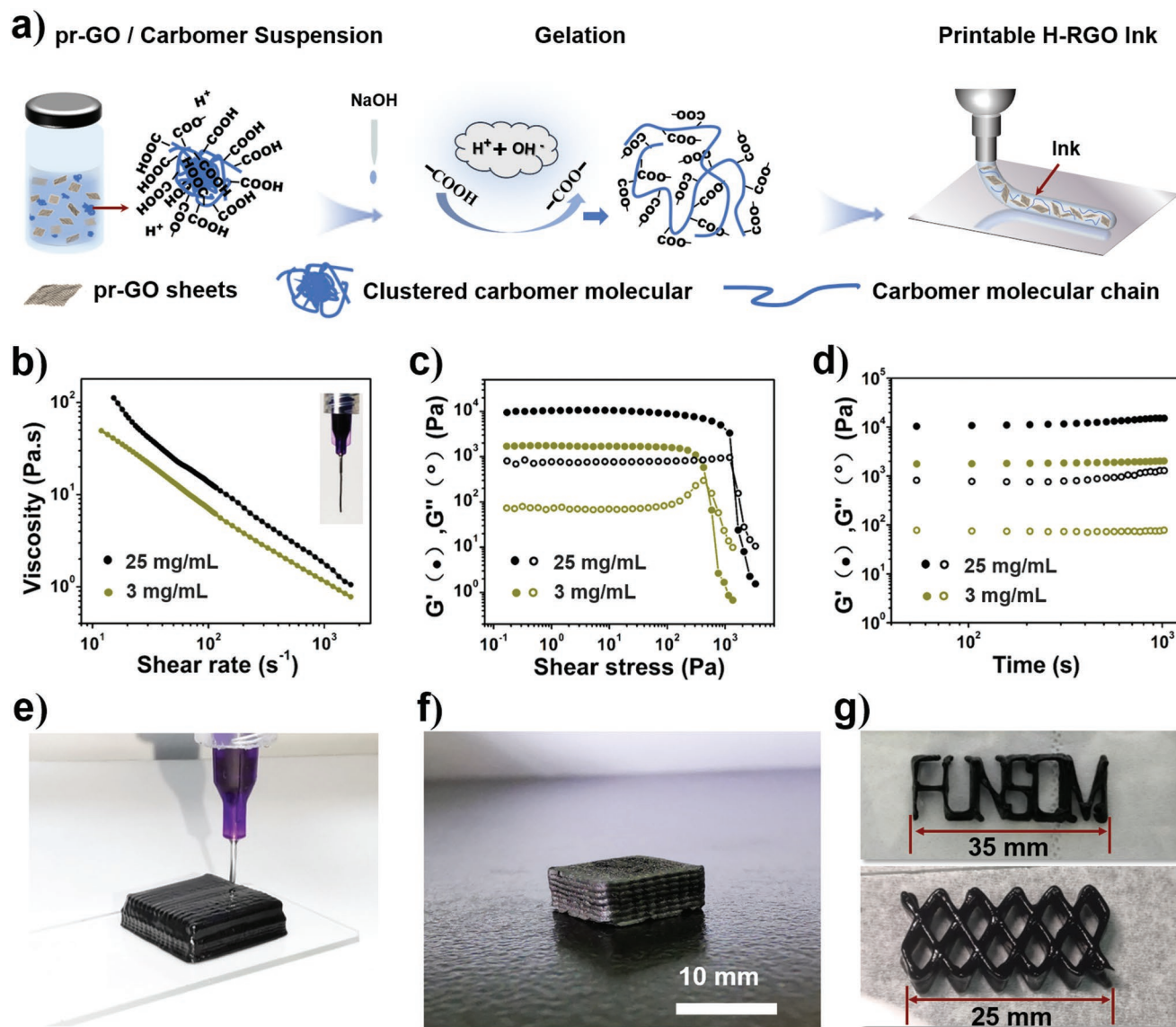


Figure 2. Preparation and rheological properties of H-RGO inks and 3D printing of laminated graphene. a) Schematically showing the preparation of H-RGO ink. b) Apparent viscosity of the H-RGO ink as a function of shear rate. c) Loss modulus (G'') and storage modulus (G') as a function of shear stress for H-RGO inks and d) their evaluation as a function of time. e) Optical image of 3D printing of laminated graphene. f) Photographs of a representative laminated graphene with length, width, and height of 10, 10, and 5 mm, respectively. g) Photographs of 3D printed graphene materials, including 3D letters (FUNSOM) and a scaffold featuring eight layers with a height of 3 mm.

printed laminated graphene materials using these two H-RGO inks (Figure 2e). Figure 2f shows a representative 3D printed laminated graphene sample with a length, width, and height of 10, 10, and 5 mm, respectively. The whole printing process was carried out in ambient air without the need for additional curing treatments, which provides excellent flexibility and convenience for printing operations. As proof of this concept, 3D letters and diamond-shaped scaffolds (Figure 2g) were printed by adapting the printing program using this H-RGO ink. Moreover, this hydrogel-based ink preparation method has good versatility for preparing other nanomaterials into 3D printable inks with good rheological properties. As a proof of concept, we prepared hydrogel-based TiO_2 ink based on such ink preparation strategy and realized 3D printing (Figure S2, Supporting Information).

The printed samples were immediately treated with liquid nitrogen to create ice-induced cellular microstructures, followed by a freeze-drying treatment to dry the samples. It has been demonstrated that many parameters of the ink, including the shape, size distribution, and density of the “particles” (solid components of the ink), can affect the interactions between the “particles” and solution, which results in changing the solidification kinetics of the freezing process and the resulting pore structure.^[58,59] In this work, the reduction degree of GO nanosheets was controlled to adjust the size and distribution of the GO nanosheets to form cellular microstructures by a freeze casting treatment. After freeze-drying, the ice is removed, and the cellular microstructure is retained in the printed graphene materials. In addition, a large amount of water in the

hydrogel-based ink allows the contact interface between the top and bottom layers printed with the two different inks to blend seamlessly. As a result, the graphene nanosheets at the interface form a continuous, seamless cellular microstructure under the extrusion of the ice crystals.

Then, the samples were further annealed at 400 °C in an Ar/H₂ atmosphere for 30 min to improve the reduction degree as well as the electrical properties of graphene. As shown in Figure S3, Supporting Information, the ratio of the intensity of the defect-induced band (I_D) and crystalline graphite band (I_G) of the annealed sample exhibits a significant decrease compared to the sample before annealing, which indicates that the heat treatment enhanced the reduction of printed graphene.^[60] During the freeze casting process, the growth of ice crystals causes the cross-linked pr-GO sheets in the H-RGO ink to form a cellular microstructure under the extrusion of ice crystals.^[58,61] It has been demonstrated that the strongly bonded cellular microstructure helps to enhance the structural stability of graphene materials,^[62] which is favorable for preparing pressure sensors with long-term device stability. In addition, to further improve the stability of the laminated graphene materials for long-term operations, an ultrathin polymer layer (PDMS) was coated on the surface of the cellular walls (Figure S4, Supporting Information). The cyclic compression test showed that the pristine printed graphene samples produced irreversible plastic deformation at 85% compressive strain (Figure S5a, Supporting Information), while the PDMS-treated samples almost completely recovered under the same compressive strain (Figure S5b, Supporting Information). In addition, we tested the stress–strain curves of three independent samples printed with the same ink, with the same shape and size, and treated by the same PDMS coating process (Figure S6, Supporting Information). The results show that the three samples have the same stress–strain properties, indicating that these PDMS coating experiments are reproducible.

The conductivities of pristine ultrathin- and thick-walled cellular samples were approximately 0.102 and 1.427 S m⁻¹, respectively, while those after PDMS coating were approximately 0.101 and 1.401 S m⁻¹, respectively. These results suggest that an ultrathin PDMS coating has no significant effect on the electrical properties of the cellular graphene materials and therefore does not introduce a new interfacial contact resistance. In addition, PDMS modification endows the printed graphene materials with good hydrophobicity (Figure S7, Supporting Information), which will be beneficial for its potential application in wet environments (e.g., wet skin with sweat or rainwater).

To mimic the synergistic strategy of the dual mechanoreceptors (touch receptors and baroreceptors) in human skin, we designed and printed a laminated graphene pressure-sensitive material using two H-RGO inks with different graphene contents. The cellular structure printed from low graphene-content ink has an ultrathin wall thickness (≈15 nm, Figure 1e top), while the cellular structure printed by high graphene-content ink features a substantially thicker wall thickness (≈117 nm, Figure 1e bottom). Compressive performance curves (Figure S8, Supporting Information) showed that the very soft ultrathin-walled cellular graphene with a Young's modulus of ≈9 kPa is expected to be able to generate significant deformation at very low applied pressures, while thick-walled cellular graphene with a Young's modulus of ≈140 kPa allows it to be able to continue to deform under very high pressure.

For piezoresistive materials, the basic theory for pressure sensing is to detect the electrical signal variation in response to mechanical deformation of the material under external pressure stimuli.^[20] The change in contact areas/points of conductive sensing materials under applied pressure significantly determines the electrical properties of the pressure sensing materials. For a piezoresistive material with only one microstructure, its resistance tends to vary approximately monotonically as the compression deformation increases. (Figure S9, Supporting Information). As a result, piezoresistive materials with only one single microstructure always lead to significant limitations in their pressure-sensing performance, such as the contradiction between the ultralow detection limit and the wide pressure detection range.

To guide the design of pressure sensing materials, finite element simulations were conducted to calculate the strain behavior of a bilayer laminated graphene. As shown in Figure 3a, at a low applied pressure (1 kPa), the top thin-walled cellular graphene produced significant strain, while the bottom thick-walled cellular graphene generated essentially no compressive strain. When the applied pressure is increased to 20 kPa, the top layer produces a large compressive strain, and the bottom layer starts to generate strain. When the applied pressure is increased to 400 kPa, the top layer is sufficiently compressed to generate no further significant strain, while the bottom graphene is still capable of generating strains. Since the compressive deformation of the material increases its microscopic contact area/points, the equivalent circuit of laminated graphene also includes the three cases corresponding to the three compressive strain stages mentioned above (Figure S10, Supporting Information). The synergy of the significantly different pressure-electrical signal response characteristics of different layers is expected to overcome the contradiction between the ultralow detection limit and the wide pressure detection range of the conventional piezoresistive materials with a single microstructure.

To evaluate the pressure-sensing performance of 3D printed laminated graphene materials, a PDMS-modified bilayer graphene sheet consisting of ultrathin-walled cellular graphene (upper layer, ≈2.5 mm) and thick-walled cellular graphene (bottom layer, ≈2.5 mm) was assembled into a piezoresistive pressure sensor. The pressure sensor has a simple sandwich structure of electrode/graphene sensing material/electrode. The simple device structure and the ability to convert pressure directly into an electrical signal, as well as ease of signal processing, are the distinct advantages of piezoresistive pressure sensors. Figure 3b shows the current–voltage (I – V) curves of the laminated graphene pressure sensor from –1 to 1 V recorded at different static pressures. The linear relationship and steady responses showed that the laminated graphene follows Ohm's law and that the resistance decreases under pressure.

Sensitivity is an essential parameter for evaluating the performance of a pressure sensor in converting the applied pressure into electrical signals. The sensitivity can be defined as $S = \delta(\Delta E/E_0)/\delta P$, where E_0 is the initial electrical signals (e.g., current, voltage, or capacitance) in the absence of applied pressure, ΔE is the variation in electrical signals, and δP is the change in applied pressure (i.e., working range).^[63–65] As shown in Figure S11, Supporting Information, the pressure sensor based

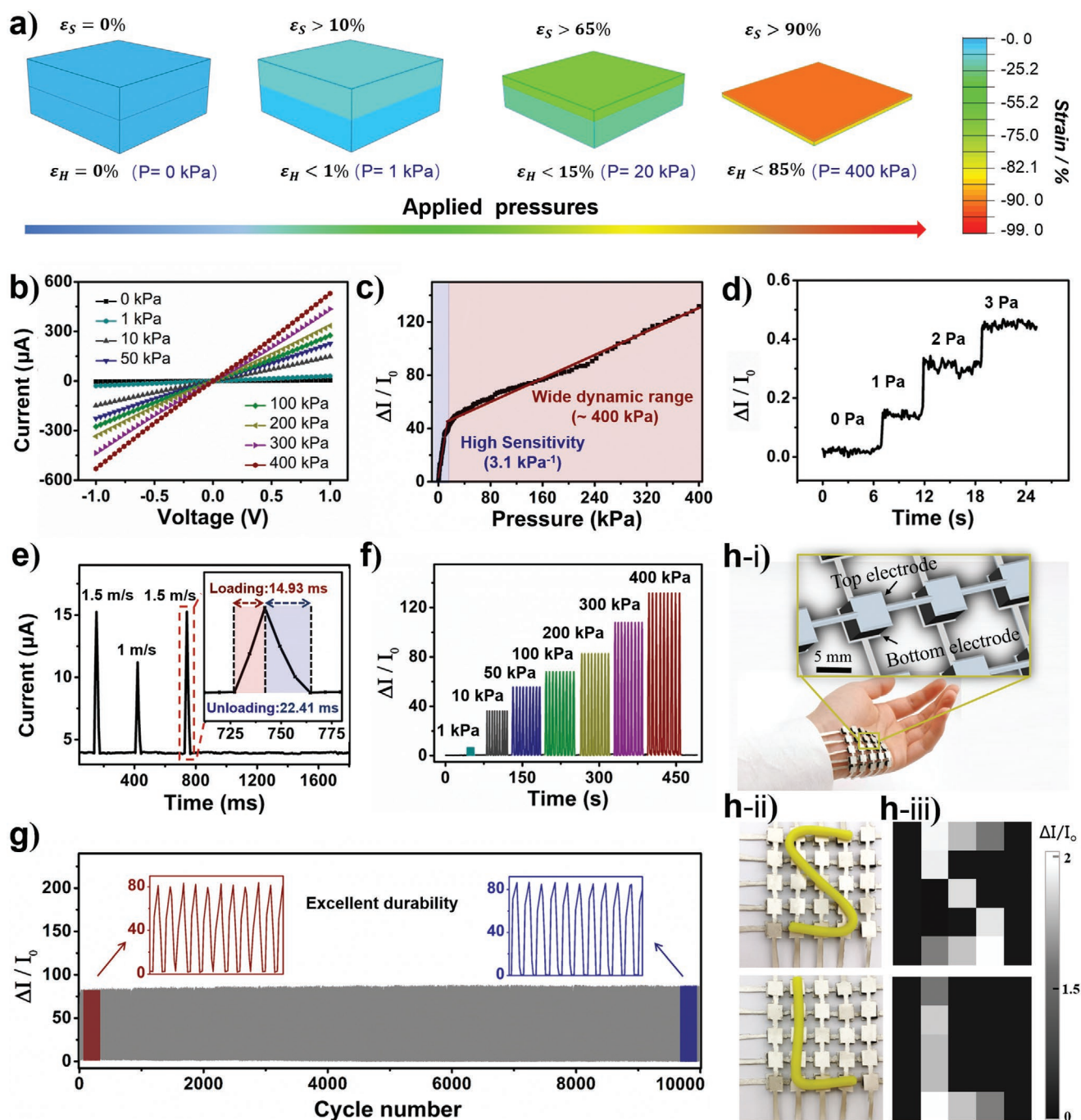


Figure 3. a) Strain calculation of laminated graphene under applied pressures, showing the responses of thin-walled (top) and thick-walled cellular layers (bottom) to different applied pressures. b) I - V curves of the pressure sensor under different applied pressures. c) Pressure-response curve for the pressure sensor, exhibiting a pressure sensitivity of $\approx 3.1 \text{ kPa}^{-1}$ in the low-pressure regime ($< 13 \text{ kPa}$) and $\approx 0.22 \text{ kPa}^{-1}$ in the high-pressure regime (13 – 400 kPa). d) The step response of the sensor with loading pressures of 1, 2, and 3 Pa. e) Pressure sensor under wind loads. f) Stable relative current variation of the pressure sensor over a wide pressure regime (1 – 400 kPa) with multiple cycles of loading/unloading. g) The reliability test of the device through 10000 loading/unloading cycles at a pressure of 200 kPa showed excellent long-term device stability. h-i) Photograph of a flexible 5×5 pressure-sensor array placed on the hand and a schematic diagram of the device structure. h-ii) Photographs of letters "S" and "L" on the surface of the pressure-sensor array. h-iii) Current mapping of pressure distributions in (h-ii).

only on thin-walled cellular graphene possesses a sensitivity of up to 3.6 kPa^{-1} in the low-pressure region ($< 19 \text{ kPa}$) and an ultralow detection limit of 1 Pa. However, the sensitivity quickly drops to a very low level (0.009 kPa^{-1}) in a high-pressure range

(19 – 400 kPa) and thus cannot be used for the sensitive detection of high pressure. In contrast, the pressure sensor based only on thick-walled cellular graphene holds a sensitivity higher than 0.1 kPa^{-1} under an applied pressure up to 400 kPa due to

the higher compressive strength of the thick-walled cellular microstructure; therefore, continuous monitoring under high pressure can be satisfied. However, the sensitivity of the device in the low-pressure range (<30 kPa) is significantly lower than that of the thin-walled cellular graphene-based device, and the minimum pressure detection limit is too high (30 Pa) to detect subtle pressure stimuli. Figure 3c presents the curve of the current change versus the pressure variation of the pressure sensor based on laminated graphene sensing materials. It can be seen that $\Delta I/I_0$ increases approximately linearly with increasing pressure in the two pressure regions. The least-squares fitting shows that the pressure sensor has high sensitivities of 3.1 and 0.22 kPa⁻¹ in the pressure regions below 13 kPa and 13–400 kPa, respectively. Figure 3d shows the step response of the pressure sensor with loading extremely low pressures of 1, 2, and 3 Pa, which demonstrates the sensor's ability to detect subtle pressures down to 1 Pa. The above results show that the different microstructural layers in laminated graphene can mimic the synergistic effect of dual mechanoreceptors in human skin, achieving a pressure detection range beyond that of human skin. Figure 3e shows that the sensor exhibits different electrical signals at wind speeds of 1 and 1.5 m s⁻¹, proving the potential for accurate airflow monitoring. In addition, the sensor features a very fast response capability with a response time of 14.93 ms and a relaxation time of 22.41 ms (inset of Figure 3e). It has been demonstrated that graphene materials with cellular microstructures have excellent resilience, which should be the key to a fast response. Due to the fast response, ultralow detection limit, and high sensitivity, the laminated graphene pressure sensing material can be readily implemented into wearable electronic devices for monitoring motion activities and physiological signals, human–machine interfacing, digital tactile systems, etc. As a proof-of-concept, we employed such a laminated graphene-based pressure sensor to monitor throat vibrations for voice recognition (Figure S12, Supporting Information). The test results show that the pressure sensor can record stationary current signals corresponding to the pronunciation of words when volunteers read the words “good”, “sensor”, and “configurations”. In addition, the sensor is able to detect differences in the current signals of different volunteers for the same pronunciation (Figure S12, Supporting Information). This result indicates that the 3D-printed laminated graphene sensing materials can be applied to wearable vibration sensors for voice recognition and voice encryption.

To evaluate the device stability of the laminated graphene-based pressure sensor, the current response at different applied pressures (1, 10, 50, 100, 200, 300, and 400 kPa) was recorded (Figure 3f). As clearly seen in Figure 3f, the sensor exhibits a stable current signal response under all applied pressures. To investigate the long-term durability of the sensing materials, 10 000 loading and unloading cycle tests were performed under a constant pressure of 200 kPa (Figure 3g). No significant change is observed in the current change amplitude during 10 000 loading and unloading cycles. The insets in Figure 3g present the magnified curve of the current change responses to the dynamic pressure at both ends of the durability test, and the identical peaks indicate good repeatability. These results suggest that the laminated graphene sensing materials have good stability and long-term durability.

Mapping detection of the position of mechanical stimuli is considered an important function needed for the practical applications of electronic skin and human-computer interfaces. To achieve the detection of the spatial pressure distribution, we prepared a flexible pressure sensor array with 5 × 5 pixels using laminated graphene (Figure 3h-i). The circuit schematic of the pressure sensor matrix is shown in Figure S13, Supporting Information. Plasticine “S” and “L” letters weighing 0.89 and 0.69 g (Figure 3h-ii), respectively, were used to test the pressure space distribution detection capability of the above pressure sensor array. The current change in each pixel was detected, and the color contrast corresponding to the loading pressure distribution is plotted in Figure 3h-iii. As clearly seen in Figure 3h-iii, the local pressure distribution can be mapped by the color contrast, which has good consistency with the shape of the letter samples. The above results show that this 3D printed laminated graphene material with a flexible and controllable shape and size has the potential to build a large-area flexible electronic skin. The ability of laminated graphite to detect high pressure enables it to be used for human motion detection. For example, it can be integrated into a device that can sensitively record the trampling action of people (Figure S14a, Supporting Information). In contrast, the ability of laminated graphene to detect very low pressure allows it to perform respiratory monitoring (Figure S14b, Supporting Information). The respiration detection mask not only detects the intensity of a person's breathing but also the respiration rate, which has great potential for monitoring the physical condition of patients/healthcare workers who need to wear masks for long periods of time.

To sensitively respond to complex external pressure stimuli and achieve precise manipulation of objects, intelligent robots need pressure-sensing skins that can quantitatively detect pressure and weight. Based on this laminated graphene, as a concept demonstration, we fabricated a small piece of pressure sensing skin that can quantify the weight in real-time over a wide detection range (Figure 4). The pressure-sensing skin mainly consists of a laminated graphene pressure sensor, an analog-to-digital converter (ADC), a micro-control unit (MCU), and a liquid crystal display (LCD) screen (Figure 4a). The ADC and MCU units are employed to convert the electrical signal to mass and display it on the LCD screen. This pressure-sensing skin can be used to quantitatively detect and display the weight of various objects ranging from extremely light soybeans to heavy adults (Figure 4b). For intelligent robots, such a pressure-sensing skin that can detect pressure/weight in real-time and quantitatively will help them to achieve precise manipulation of objects. In addition, the low detection limits and wide detection ranges are of particular demand for wearable electronics to enable human motions and physiological signal monitoring.

3. Conclusion

In summary, skin-inspired laminated graphene pressure sensing materials, consisting of both a soft ultrathin-walled cellular layer with a very low elastic modulus and a relatively stiff thick-walled cellular layer with a higher elastic modulus are designed and printed. The ultrathin-walled cellular microstructure (functioning as the touch receptor in human skin)

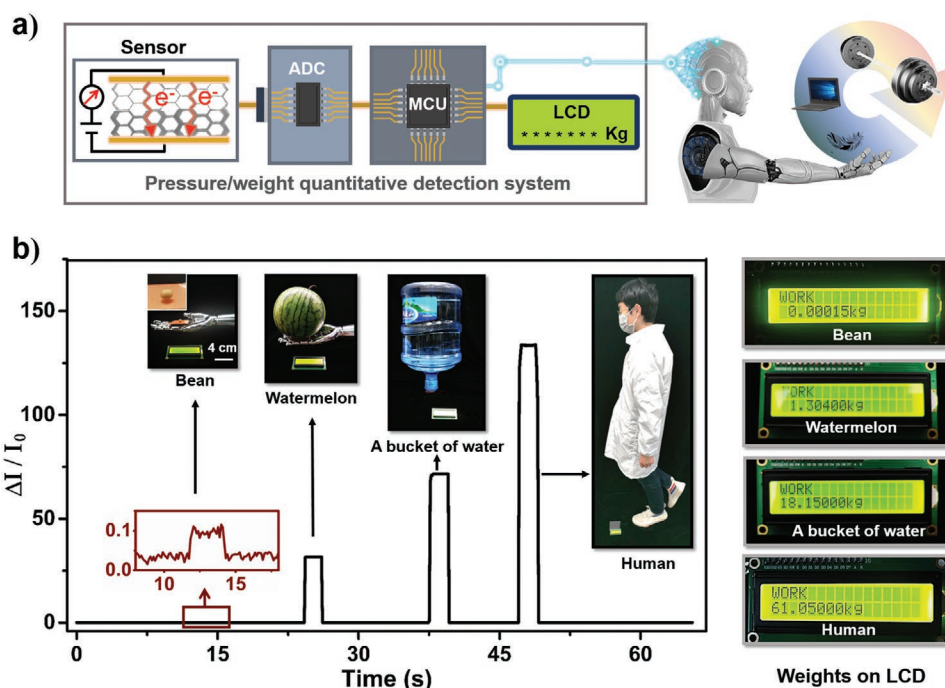


Figure 4. Weight quantitative detection devices integrated by 3D printed laminated graphene pressure sensing material. a) Schematic diagram of the device system. b) The current signals corresponding to different objects (left) and the displays of the weight indications (right).

is explored to sense subtle pressure due to its very low elastic modulus, while the thick-walled cellular structure with a high elastic modulus is used to serve as the baroreceptor in the skin to detect large pressure stimuli. Pressure sensors prepared using such laminated sensing materials achieve both extremely low detection limits down to 1 Pa, a wide detection range (1 Pa–400 kPa), and high sensitivities of 3.1 and 0.22 kPa⁻¹ in the low (1 Pa–13 kPa) and high (13–400 kPa) pressure regimes, respectively. In addition, the cellular microstructure and PDMS-coating treatment impart the laminated graphene features excellent durability for over 10 000 operations. Moreover, this laminated graphene pressure-sensing material demonstrates the feasibility of being integrated into flexible and large-area electronic skins. The robot skin prepared based on this laminated graphene demonstrated the ability to quantitatively detect and display weight/pressure over a wide range. This skin-inspired material structure design concept combined with a flexible ink-based 3D printing strategy provides a promising way for the development of high-performance pressure sensing devices for intelligent robots. In addition, this 3D printed pressure sensing material can be readily used in various applications, such as physiological conditions and motion activity monitoring, where both low detection limits and wide detection ranges are needed.

4. Experimental Section

Materials: The graphite flakes (XF049, 50 mesh) for the preparation of GO nanosheets were purchased from XFANO Inc. Fuming nitric acid (HNO₃), concentrated H₂SO₄ (98%) and ethyl acetate (99.5%) were purchased from Chinasun Specialty Products Co., Ltd. KMnO₄, P₂O₅, K₂S₂O₈, and H₂O₂ (30%) solutions were purchased from Sinopharm Chemical Reagent Co., Ltd. AA and carbomer were purchased from

Sigma Aldrich. PDMS (SYLGARD 184 SILICONE) was purchased from Dow Chemical Company. All the materials and reagents were used as received without further purification.

Ink Preparation: A GO aqueous solution (≈5 mg mL⁻¹) containing large GO nanosheets with large lateral dimensions ranging from several microns to dozens of microns was prepared according to the method reported in the previous literature. The GO aqueous solution was reduced to pr-GO at 80 °C for 10 min by adding a weak reductant AA solution (0.45 mol mL⁻¹), and the mass ratio of GO to AA was kept at ≈3:1. Then, the excess AA was washed off with distilled water. Then, the swelled carbomer was uniformly mixed into the pr-GO aqueous solution (3 and 25 mg mL⁻¹), and the content of carbomer in the mixed solution was maintained at 1 wt%. Finally, NaOH (20 mg mL⁻¹) was used to adjust the rheological properties of the solution to meet the requirements of extrusion-based 3D printing.

3D Printing: The squeezable ink was printed onto a glass substrate using an industrial robotic dispenser (Fisnar F5200n) with the capability of programming 3D patterns. The maximum resolution of the mechanical arm of the printer is 1 μm per axis. Prior to printing, the ink was loaded into a Fisnar syringe barrel (30 mL) fitted with a pneumatic piston and stainless-steel nozzle with a diameter of 510 μm. The printing pressure and moving speed of the nozzle can be adjusted at will. Then, the pressure sensors were directly printed by assembling the pr-GO filaments through a layer-by-layer build subsequence. The whole 3D printing process was performed in an ambient air environment without the need for any in situ solidification treatments. The printed sample was immediately frozen to obtain the cellular microstructure. The printed samples were immediately treated with liquid nitrogen to create ice-induced cellular microstructures, followed by a freeze-drying treatment to remove moisture. Then, the dried samples were heat-treated at 400 °C in an Ar/H₂ atmosphere for 30 min to further reduce GO. The heating and cooling rates of the heat treatment of the 3D printed pr-GO body were set to 2 °C min⁻¹.

Preparation of Pressure Sensing Devices: The annealed graphene material was impregnated with a diluent of PDMS polymer, and the impregnating solution was prepared according to the ratio of M(ethyl acetate):M(base silicone gel):M(curing agent) = 100:10:1. The samples were soaked for 30 min, and the upper and lower electrodes were then assembled. Then, the

samples were cured in an oven at 100 °C for 30 min. Finally, a piezoresistive pressure sensor with stable compression performance was prepared.

Characterizations: The rheological properties of the H-RGO ink were characterized in an ambient environment using a stress-controlled Rheometer (Kinexus pro, Malvern) with a 40-mm flat plate geometry (gap width of 1 mm). The apparent viscosity of the H-RGO ink was recorded in a shear rate range of $1\text{--}10^3\text{ s}^{-1}$. Oscillatory measurements were recorded at a constant frequency of 1 Hz. The morphology of GO nanosheets and 3D printed laminated graphene were characterized by a Veeco atomic force microscope (AFM), an FEI Tecnai F20 transmission electron microscope (TEM), and a ZEISS scanning electron microscope (SEM). The TEM samples of cellular graphene were prepared by sectioning the graphene samples into ultrathin slices with a thickness of $\approx 1\text{ }\mu\text{m}$ and transferring them to a support film. The compressive characteristics were measured using a universal testing machine (Instron 3365). The electrical conductivities of graphene-based materials were measured on the basis of a four-point probe resistance measurement system (ST-2258C, Suzhou Jingge Electronic Co., Ltd.). The Raman spectra were measured using a LabRAM ARAMIS Raman confocal microscope (Aramis CRM, Horiba Jobin-Yvon, Edison, NJ) with 532 nm laser excitation from 400 to 4000 cm^{-1} . The static contact angle was measured using an optical contact angle measuring instrument (Dataphysics, OCA15EC, Germany) at room temperature, and the volume of the water droplet was 3 μL . In the characterizations of the pressure sensor, the applied force was measured by the Chatillon DFS force measurement (AMETEK Co., Ltd.). The current signals of the pressure sensor under wind loading were measured using an air gun. The air gun was fixed so that its nozzle was perpendicular to the electrode surface of the pressure sensor, and the wind speed was measured with an anemometer (Testo 405-V1). The current signal of the devices was measured by a multi-parameter measuring instrument (Keithley, 4200-SCS). All the experiments on human skin were performed under the protocol approved by Ethics Committee of Soochow University. And, prior to the skin adhesion experiments, volunteers in this study provided their written informed consent.

Mechanistic Modeling: The compression of the graphene cellular structure and the associated deformation/stress were modeled by using the commercial finite element code ABAQUS 6. 14.

The nonlinear mechanical behaviors of graphene cellular structures can be well captured by the hyperfoam constitutive model, in which the strain energy function takes the form

$$U = \frac{2\mu}{\alpha^2} \left[\lambda_1^\alpha + \lambda_2^\alpha + \lambda_3^\alpha - 3 + \frac{1}{\beta} \left[(\lambda_1 \lambda_2 \lambda_3)^{-\alpha\beta} - 1 \right] \right] \quad (1)$$

where λ_1 , λ_2 , and λ_3 are principal stretches, and μ , α , and β are material constants. Note that β is related to Poisson's ratio ν by

$$\beta = \frac{\nu}{1-2\nu} \quad (2)$$

Since the graphene cellular structure demonstrated negligible lateral strain during compression, Poisson's ratio $\nu = 0$ was set for both the thick-walled cellular structure layer and the ultrathin-walled cellular structure layer, so that the material constant $\beta = 0$ for both layers. To calibrate the material constants μ and α of the relatively hard thick-walled cellular structure layer and the soft ultrathin-walled cellular structure layer, the compression of the soft and hard layers were modeled separately and the modeling results fitted to the stress-strain curves measured in the experiments. Each individual layer was modeled as a 3D solid meshed with the C3D8R element.

The compression of the double-layer graphene cellular structure was simulated by using model constants obtained from the single-layer modeling. Again, the double-layer structure was simulated as a 3D solid that was meshed using the C3D8R element. The strain/stress distribution and the overall stress-strain curve of the double-layer graphene cellular structure could be extracted from the simulation.

Supporting Information

Supporting Information is available from the Wiley Online Library or from the author.

Acknowledgements

This work was supported by the National Natural Science Foundation of China (nos. 21822202 and 22072104). This was also a project funded by CIC, the 111 project, Joint International Research Laboratory of Carbon-Based Functional Materials and Devices, and the Collaborative Innovation Center of Suzhou Nano Science and Technology.

Conflict of Interest

The authors declare no conflict of interest.

Author Contributions

K.C. and M.W. contributed equally to this work. All authors have given approval to the final version of the manuscript.

Data Availability Statement

The data that support the findings of this study are available from the corresponding author upon reasonable request.

Keywords

3D printing, bioinspired laminated graphene, low detection limit, pressure sensing materials, wide detection range

Received: February 28, 2022

Revised: March 24, 2022

Published online:

- [1] C. M. Boutry, M. Negre, M. Jorda, O. Vardoulis, A. Chortos, O. Khatib, Z. Bao, *Sci. Robot.* **2018**, *3*, eaau6914.
- [2] Q. Zheng, J.-h. Lee, X. Shen, X. Chen, J.-K. Kim, *Mater. Today* **2020**, *36*, 158.
- [3] Y. Zhao, W. Gao, K. Dai, S. Wang, Z. Yuan, J. Li, W. Zhai, G. Zheng, C. Pan, C. Liu, C. Shen, *Adv. Mater.* **2021**, *33*, 2102332.
- [4] X. Wang, L. Dong, H. Zhang, R. Yu, C. Pan, Z. L. Wang, *Adv. Sci.* **2015**, *2*, 1500169.
- [5] S. Wang, J. Xu, W. Wang, G. N. Wang, R. Rastak, F. Molina-Lopez, J. W. Chung, S. Niu, V. R. Feig, J. Lopez, T. Lei, S. K. Kwon, Y. Kim, A. M. Foudeh, A. Ehrlich, A. Gasperini, Y. Yun, B. Murmann, J. B. Tok, Z. Bao, *Nature* **2018**, *555*, 83.
- [6] S. Nayak, Y. Li, W. Tay, E. Zamburg, D. Singh, C. Lee, S. J. A. Koh, P. Chia, A. V.-Y. Thean, *Nano Energy* **2019**, *64*, 103912.
- [7] M. Zhu, Z. Sun, Z. Zhang, Q. Shi, T. He, H. Liu, T. Chen, C. Lee, *Sci. Adv.* **2020**, *6*, eaaz8693.
- [8] J. Zhu, M. Zhu, Q. Shi, F. Wen, L. Liu, B. Dong, A. Haroun, Y. Yang, P. Vachon, X. Guo, T. He, C. Lee, *EcoMat* **2020**, *2*, e12058.
- [9] M. Zhu, T. He, C. Lee, *Appl. Phys. Rev.* **2020**, *7*, 031305.
- [10] A. Zimmerman, L. Bai, D. D. Ginty, *Science* **2014**, *346*, 950.
- [11] K. Marshall, A. Patapoutian, *Science* **2020**, *368*, 1311.
- [12] N. Luo, Y. Huang, J. Liu, S. C. Chen, C. P. Wong, N. Zhao, *Adv. Mater.* **2017**, *29*, 1702675.
- [13] Z. Lou, S. Chen, L. Wang, K. Jiang, G. Shen, *Nano Energy* **2016**, *23*, 7.
- [14] G. Yang, M.-Z. Tian, P. Huang, Y.-F. Fu, Y.-Q. Li, Y.-Q. Fu, X.-Q. Wang, Y. Li, N. Hu, S.-Y. Fu, *Carbon* **2021**, *173*, 736.
- [15] Y. Zang, F. Zhang, C.-a. Di, D. Zhu, *Mater. Horiz.* **2015**, *2*, 140.

- [16] L. Q. Tao, K. N. Zhang, H. Tian, Y. Liu, D. Y. Wang, Y. Q. Chen, Y. Yang, T. L. Ren, *ACS Nano* **2017**, *11*, 8790.
- [17] S. Sharma, A. Chhetry, S. Zhang, H. Yoon, C. Park, H. Kim, M. Sharifuzzaman, X. Hui, J. Y. Park, *ACS Nano* **2021**, *15*, 4380.
- [18] M. Wang, Y. Luo, T. Wang, C. Wan, L. Pan, S. Pan, K. He, A. Neo, X. Chen, *Adv. Mater.* **2021**, *33*, 2003014.
- [19] Z. Shen, X. Zhu, C. Majidi, G. Gu, *Adv. Mater.* **2021**, *33*, 2102069.
- [20] W. Chen, X. Yan, *J. Mater. Sci. Technol.* **2020**, *43*, 175.
- [21] H. Tian, Y. Shu, X. F. Wang, M. A. Mohammad, Z. Bie, Q. Y. Xie, C. Li, W. T. Mi, Y. Yang, T. L. Ren, *Sci. Rep.* **2015**, *5*, 8603.
- [22] J. Sha, Y. Li, R. V. Salvatierra, T. Wang, P. Dong, Y. Ji, S. K. Lee, C. Zhang, J. Zhang, R. H. Smith, P. M. Ajayan, J. Lou, N. Zhao, J. M. Tour, *ACS Nano* **2017**, *11*, 6860.
- [23] L. Duan, D. R. D'Hooge, L. Cardon, *Prog. Mater. Sci.* **2020**, *114*, 100617.
- [24] J. Qin, L. J. Yin, Y. N. Hao, S. L. Zhong, D. L. Zhang, K. Bi, Y. X. Zhang, Y. Zhao, Z. M. Dang, *Adv. Mater.* **2021**, *33*, 2008267.
- [25] J. An, P. Chen, Z. Wang, A. Berbille, H. Pang, Y. Jiang, T. Jiang, Z. L. Wang, *Adv. Mater.* **2021**, *33*, 2101891.
- [26] H. B. Yao, J. Ge, C. F. Wang, X. Wang, W. Hu, Z. J. Zheng, Y. Ni, S. H. Yu, *Adv. Mater.* **2013**, *25*, 6692.
- [27] S. R. A. Ruth, L. Beker, H. Tran, V. R. Feig, N. Matsuhisa, Z. Bao, *Adv. Funct. Mater.* **2019**, *30*, 1903100.
- [28] S. C. Mannsfeld, B. C. Tee, R. M. Stoltenberg, C. V. Chen, S. Barman, B. V. Muir, A. N. Sokolov, C. Reese, Z. Bao, *Nat. Mater.* **2010**, *9*, 859.
- [29] Y.-C. Huang, Y. Liu, C. Ma, H.-C. Cheng, Q. He, H. Wu, C. Wang, C.-Y. Lin, Y. Huang, X. Duan, *Nat. Electron.* **2020**, *3*, 59.
- [30] B. Zhu, Z. Niu, H. Wang, W. R. Leow, H. Wang, Y. Li, L. Zheng, J. Wei, F. Huo, X. Chen, *Small* **2014**, *10*, 3625.
- [31] G. Li, D. Chen, C. Li, W. Liu, H. Liu, *Adv. Sci.* **2020**, *7*, 2000154.
- [32] H. Yao, T. Sun, J. S. Chiam, M. Tan, K. Y. Ho, Z. Liu, B. C. K. Tee, *Adv. Funct. Mater.* **2021**, *31*, 2008650.
- [33] Y. Pang, K. Zhang, Z. Yang, S. Jiang, Z. Ju, Y. Li, X. Wang, D. Wang, M. Jian, Y. Zhang, R. Liang, H. Tian, Y. Yang, T. L. Ren, *ACS Nano* **2018**, *12*, 2346.
- [34] C. B. Huang, S. Witomska, A. Aliprandi, M. A. Stoeckel, M. Bonini, A. Ciesielski, P. Samori, *Adv. Mater.* **2019**, *31*, 1804600.
- [35] M. Liu, X. Pu, C. Jiang, T. Liu, X. Huang, L. Chen, C. Du, J. Sun, W. Hu, Z. L. Wang, *Adv. Mater.* **2017**, *29*, 1703700.
- [36] H. Zhuo, Y. Hu, X. Tong, Z. Chen, L. Zhong, H. Lai, L. Liu, S. Jing, Q. Liu, C. Liu, X. Peng, R. Sun, *Adv. Mater.* **2018**, *30*, 1706705.
- [37] J. He, P. Xiao, W. Lu, J. Shi, L. Zhang, Y. Liang, C. Pan, S.-W. Kuo, T. Chen, *Nano Energy* **2019**, *59*, 422.
- [38] L. Shi, Z. Li, M. Chen, Y. Qin, Y. Jiang, L. Wu, *Nat. Commun.* **2020**, *11*, 3529.
- [39] X. M. Wang, L. Q. Tao, M. Yuan, Z. P. Wang, J. Yu, D. Xie, F. Luo, X. Chen, C. Wong, *Nat. Commun.* **2021**, *12*, 1776.
- [40] C. Zhu, T. Y. Han, E. B. Duoss, A. M. Golobic, J. D. Kuntz, C. M. Spadaccini, M. A. Worsley, *Nat. Commun.* **2015**, *6*, 6962.
- [41] B. Yao, S. Chandrasekaran, J. Zhang, W. Xiao, F. Qian, C. Zhu, E. B. Duoss, C. M. Spadaccini, M. A. Worsley, Y. Li, *Joule* **2019**, *3*, 459.
- [42] J. Zhao, Y. Zhang, X. Zhao, R. Wang, J. Xie, C. Yang, J. Wang, Q. Zhang, L. Li, C. Lu, Y. Yao, *Adv. Funct. Mater.* **2019**, *29*, 1900809.
- [43] B. Yao, S. Chandrasekaran, H. Zhang, A. Ma, J. Kang, L. Zhang, X. Lu, F. Qian, C. Zhu, E. B. Duoss, C. M. Spadaccini, M. A. Worsley, Y. Li, *Adv. Mater.* **2020**, *32*, 1906652.
- [44] S. D. Lacey, D. J. Kirsch, Y. Li, J. T. Morgenstern, B. C. Zarket, Y. Yao, J. Dai, L. Q. Garcia, B. Liu, T. Gao, S. Xu, S. R. Raghavan, J. W. Connell, Y. Lin, L. Hu, *Adv. Mater.* **2018**, *30*, 1705651.
- [45] J. O. Carnali, M. S. Naser, *Colloid Polym. Sci.* **1992**, *270*, 183.
- [46] W. S. Hummers Jr, R. E. Offeman, *J. Am. Chem. Soc.* **1958**, *80*, 1339.
- [47] M. Peng, Z. Wen, L. Xie, J. Cheng, Z. Jia, D. Shi, H. Zeng, B. Zhao, Z. Liang, T. Li, L. Jiang, *Adv. Mater.* **2019**, *31*, 1902930.
- [48] L. Qiu, M. B. Coskun, Y. Tang, J. Z. Liu, T. Alan, J. Ding, V. T. Truong, D. Li, *Adv. Mater.* **2016**, *28*, 194.
- [49] F. Wang, Y. Wang, W. Zhan, S. Yu, W. Zhong, G. Sui, X. Yang, *Chem. Eng. J.* **2017**, *320*, 539.
- [50] S. Lee, Y. Song, Y. Ko, Y. Ko, J. Ko, C. H. Kwon, J. Huh, S. W. Kim, B. Yeom, J. Cho, *Adv. Mater.* **2020**, *32*, 1906460.
- [51] H. Luo, Y. V. Kaneti, Y. Ai, Y. Wu, F. Wei, J. Fu, J. Cheng, C. Jing, B. Yuliarto, M. Eguchi, J. Na, Y. Yamauchi, S. Liu, *Adv. Mater.* **2021**, *33*, 2007318.
- [52] B. Guo, G. Liang, S. Yu, Y. Wang, C. Zhi, J. Bai, *Energy Storage Mater.* **2021**, *39*, 146.
- [53] Y. Wang, C. Chen, H. Xie, T. Gao, Y. Yao, G. Pastel, X. Han, Y. Li, J. Zhao, K. K. Fu, L. Hu, *Adv. Funct. Mater.* **2017**, *27*, 1703140.
- [54] V. G. Rocha, E. Saiz, I. S. Tirichenko, E. García-Tuñón, *J. Mater. Chem. A* **2020**, *8*, 15646.
- [55] Z. Liang, Y. Pei, C. Chen, B. Jiang, Y. Yao, H. Xie, M. Jiao, G. Chen, T. Li, B. Yang, L. Hu, *ACS Nano* **2019**, *13*, 12653.
- [56] W. Guo, Y. Liu, Y. Sun, Y. Wang, W. Qin, B. Zhao, Z. Liang, L. Jiang, *Adv. Funct. Mater.* **2021**, *31*, 2100768.
- [57] Z. Liang, Y. Yao, B. Jiang, X. Wang, H. Xie, M. Jiao, C. Liang, H. Qiao, D. Kline, M. R. Zachariah, L. Hu, *Adv. Funct. Mater.* **2021**, *31*, 2102994.
- [58] Y. Shao, M. F. El-Kady, C. W. Lin, G. Zhu, K. L. Marsh, J. Y. Hwang, Q. Zhang, Y. Li, H. Wang, R. B. Kaner, *Adv. Mater.* **2016**, *28*, 6719.
- [59] Q. Cheng, C. Huang, A. P. Tomsia, *Adv. Mater.* **2017**, *29*, 1703155.
- [60] L. M. Malard, M. A. Pimenta, G. Dresselhaus, M. S. Dresselhaus, *Phys. Rep.* **2009**, *473*, 51.
- [61] J. Cao, X. Zhao, J. Wang, H. Dou, C. Liu, X. Yan, Y. Yan, M. Guo, W. Zhao, X. Yang, *Chin. Chem. Lett.* **2020**, *31*, 265.
- [62] L. Qiu, J. Z. Liu, S. L. Chang, Y. Wu, D. Li, *Nat. Commun.* **2012**, *3*, 1241.
- [63] X. Li, Y. J. Fan, H. Y. Li, J. W. Cao, Y. C. Xiao, Y. Wang, F. Liang, H. L. Wang, Y. Jiang, Z. L. Wang, G. Zhu, *ACS Nano* **2020**, *14*, 9605.
- [64] D. Lee, H. Lee, Y. Jeong, Y. Ahn, G. Nam, Y. Lee, *Adv. Mater.* **2016**, *28*, 9364.
- [65] Z. Wang, S. Guo, H. Li, B. Wang, Y. Sun, Z. Xu, X. Chen, K. Wu, X. Zhang, F. Xing, L. Li, W. Hu, *Adv. Mater.* **2019**, *31*, e1805630.